PROGRESS IN PHOTOVOLTAICS: RESEARCH AND APPLICATIONS
Prog. Photovolt: Res. Appl. 2011; **18**:517–526
Published online 5 January 2011 in Wiley Online Library (wileyonlinelibrary.com). DOI: 10.1002/pip.1076

RESEARCH ARTICLE

A genuine circular contact grid pattern for solar cells

G.M.M.W. Bissels*, M.A.H. Asselbergs, J.J. Schermer, E.J. Haverkamp, N.J. Smeenk and E. Vlieg

Radboud University Nijmegen, Institute for Molecules and Materials, Heyendaalseweg 135, 6525 AJ Nijmegen, the Netherlands

ABSTRACT

A model was developed for a genuine circular contact grid, based on the same principles that led to previously reported models for other contact grid types. The circular grid differs from the regular (radial) grid often applied to round solar cells, in that it has considerably less radial lines and many more concentric rings, to the effect that the rings now take on the role of fingers, while the lines serve as busbars. For a 16 mm^2 n-on-p GaAs cell and irradiances ranging from 1 to 1000 suns, optimised grids of this new circular design were compared to equivalent radial, square and inverted square grids. Furthermore, in order to allow for a fair comparison of the different grid types, the previously reported radial grid model was modified to obtain additional freedom in design that is comparable to that of the other grid configurations. The circular grid turned out to suffer less power loss than a comparable radial grid up to a concentration ratio of 30. At higher concentration ratios, cells with a radial grid performed better, while comparable square and inverted square grids perform better over the entire range of concentration ratios. For GaAs cells serving as the bottom cell in a mechanical tandem, the effects of secondary shadowing were calculated for a range of translational and rotational misalignments, for the four patterns optimised for the case where the GaAs cell is effectively subjected to a concentration ratio of 500. The effects of translational misalignment varied little between the grids, but the rotational misalignment effects demonstrated the strength of the circular grid, since its shadowing loss hardly increases with increasing rotational misalignment angle, while those of the other three grid types quickly approach a doubling. When these secondary shadowing effects are taken into account, the circular grid can be the preferred pattern for the constituent cells of a mechanical stack, depending on the accuracy with which those cells can be rotationally aligned. Copyright © 2011 John Wiley & Sons, Ltd.

KEYWORDS

circular contact grid pattern; mechanical stacking; multi-junction concentrator solar cell

***Correspondence**

G.M.M.W. Bissels, Radboud University Nijmegen, Institute for Molecules and Materials, Heyendaalseweg 135, 6525 AJ Nijmegen, the Netherlands.

E-mail: G.Bissels@science.ru.nl

Received 21 May 2010; Revised 16 September 2010

1. INTRODUCTION

For concentrator systems, the performance of a solar cell is of major importance, so multi-junction III–V cells are the standard in the quest for ever higher efficiencies. So far, the highest efficiency is obtained using a monolithic triple-junction cell [1,2], and efforts are made to top this by adding a good quality fourth junction with the proper bandgap. This proves to be very difficult, however, due to lattice- and current-matching restrictions. One way to circumvent these restrictions is to use a combination of monolithic and mechanical stacking [3–7].

In a mechanical stack, the contact grids of the constituent solar cells should be aligned in order to minimise secondary shadowing losses in the lower cell(s), i.e. shadowing by the grid of the higher cell(s). This requires both lateral (in two directions) and rotational alignment. In our laboratory the optical losses associated with misalignment of the cells is investigated experimentally using semi-transparent InGaP and GaAs top cells as obtained with the epitaxial lift-off technique [8,9], and GaAs as well as crystalline Si bottom cells. Preliminary results of these investigations show that the rotational alignment is the most challenging factor of the threefold alignment, and is limited to an accuracy of about 0.3° with our current setup. In an effort to optimise the process window for mechanical stacking, one might conceive a contact grid design that is less sensitive to rotational misalignment than the regularly used contact grids. The regular grid designed for round cells consists of a large number of radial fingers which branch out at a few selected radii,

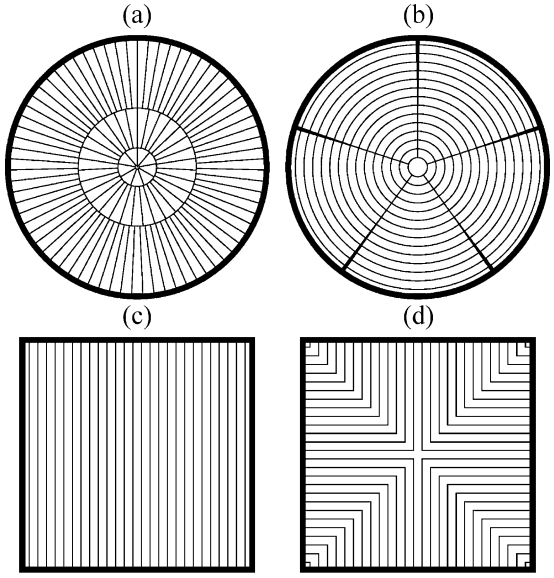

Figure 1. Schematic representation of (a) a radial grid, (b) a circular grid, (c) a square grid and (d) an inverted square grid. The thick frames surrounding the cells represent the collectors.

using circular busbars. An example of such a grid, which will be referred to as *radial* grid in this work, is displayed in Figure 1a. A rotational misalignment of two cells with such a grid results in a large secondary shadowing loss for the bottom cell. If the (radial) fingers are bunched into only a few bands, though, this secondary loss could drop significantly for relatively small rotational misalignments. This would, however, raise the resistive power loss due to the increased average path length for the electrons through the solar cell's top layer towards the metal grid. Therefore, additional grid rings are introduced, resulting in a genuine *circular* contact grid as shown in Figure 1b. Since most of the cell's surface is now closer to one of the rings than one of the radial lines, the rings take on the role of fingers, while the radial lines take on the role of busbars, so their roles are reversed with respect to the radial grid. This means the model to describe the performance and determine the optimum configuration of the radial grid is not suited to be applied to the here proposed circular grid, so a new model was developed in the present study. This was done along the lines of Moore's model for the *inverted square* grid [10], Green's model for the *square* grid [11] and Algora and Díaz' model for the radial grid [12].

Using the new model, it was evaluated under which circumstances this circular grid design would be a viable alternative for the regularly applied grid types. For this purpose, the total relative power loss induced by the circular grid was compared to that induced by the radial, square (Figure 1c) and inverted square (Figure 1d) grid types. In order to obtain a fair comparison, it is essential to apply models that are mathematically developed to a level that allows for the same degree of freedom in design as the here introduced circular contact grid. For this purpose the inverted grid model that allows for non-uniform finger spacing [10] is applied and the originally derived radial grid model [12] is developed in such a way that the pre-set relations on the number of fingers per annulus and distribution of its busbar radii can be omitted. Using these models, all contact grids are individually optimised for each specific condition. For this, the cells are considered to have the same constant finger width and surface area, and have a collector surrounding the entire cell lying outside this surface area, which is common for concentrator cells.

2. THEORY

Apart from shadowing losses, a solar cell typically suffers relevant power losses from three electrical resistances: top layer resistance towards the fingers, contact resistance at the fingers and metal resistance loss in the fingers and busbars. Expressions for these four power loss components are derived here for the circular grid, based on the same principles that led to previously reported models for other contact grid types [10–12]. This means that the contact resistance of the busbars is taken as infinite, so the generated current is only extracted via the fingers and not directly via the busbars.

The circular contact grid, composed of n radial busbars and m circular fingers, can be broken down into $2n$ pie-slice shaped unit cells like the one depicted in Figure 2, in which the current is directed to one-half of a busbar. Each unit cell consists of m segments, each composed of a section of an annulus with a finger approximately in its centre. Note that, unlike the square and radial grid types, the finger distance is not constant and the ideal finger radii will follow from the model. The model, therefore, requires a more laborious mathematical derivation, with the introduction of the radii of the segments ρ_i as initially unknown functions of the finger radii. Based on the variables defined in Figure 2, the derivation of the relative power loss components is given below, first for the fingers and then for the busbars. In addition, the model of Algora and Díaz [12] for the radial contact grid is modified in such a way that it allows for a fair comparison with the other grid models considered here.

2.1. Losses due to the fingers

2.1.1. Top layer resistance loss towards the fingers.

Consider the inner part of segment i, ranging from ρ_{i-1} to r_i. The current generated in this area will flow through the top layer of the solar cell, radially outwards towards the finger with radius r_i. The current I increases with radius r according to

$$I(r) = J_{\mathrm{mp}} \frac{\pi}{2n} \left(r^2 - \rho_{i-1}^2\right) \tag{1}$$

where J_{mp} is the current density of the solar cell at the maximum power point. The resistance through the top layer

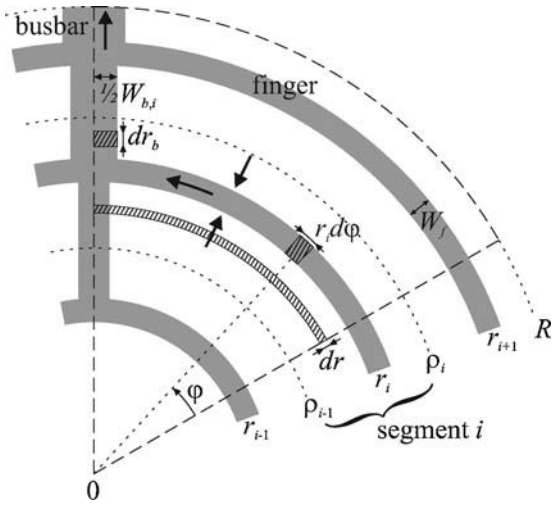

Figure 2. Schematic representation of one of the 2*n* pie slice shaped unit cells (boundaries marked by the dashed lines) that make up the entire circular contact grid.

of the solar cell in the ring section of width dr equals

$$\mathrm{d}R_{\mathrm{tf}} = \rho_{\mathrm{st}}\frac{n}{\pi r}\mathrm{d}r \tag{2}$$

where ρ_{st} is the sheet resistance of the top layer. The power loss due to top layer resistance in the area of interest can then be calculated to be

$$\begin{aligned} P_{\mathrm{tf},i,\mathrm{inner}} &= \int_{\rho_{i-1}}^{r_i} I^2(r)\mathrm{d}R_{\mathrm{tf}} \\ &= \frac{\pi}{4n}J_{\mathrm{mp}}^2\rho_{\mathrm{st}}\left(\frac{1}{4}r_i^4-\rho_{i-1}^2r_i^2\right. \\ &\quad \left.+\rho_{i-1}^4\left[\ln\left(\frac{r_i}{\rho_{i-1}}\right)+\frac{3}{4}\right]\right) \end{aligned} \tag{3}$$

By adding the power loss in the outer part of this segment, the total power loss of segment i, $P_{\mathrm{tf},i}$, is obtained. p_{tf}, the relative power loss due to top layer resistance, can then be found by summing the power losses of all the segments and dividing it by the total power generated by the unit cell.

$$P_{\mathrm{gen}} = J_{\mathrm{mp}}V_{\mathrm{mp}}\frac{\pi R^2}{2n} \tag{4}$$

with V_{mp}, the cell's maximum power point voltage and R, the radius of the cell. This gives

$$\begin{aligned} p_{\mathrm{tf}} &= \frac{J_{\mathrm{mp}}\rho_{\mathrm{st}}}{2V_{\mathrm{mp}}R^2}\left[R^4\left[\ln\left(\frac{\mathrm{R}}{\mathrm{r_{m+1}}}\right)-\frac{3}{4}\right]\right. \\ &\quad \left.+\sum_{i=1}^{m}\left(\rho_i^4\ln\left(\frac{r_{i+1}}{r_i}\right)+\left(\rho_i^2-\rho_{i-1}^2\right)r_i^2\right)\right] \\ &\equiv \lambda_{\mathrm{tf}}\left[R^4\left[\ln\left(\frac{R}{r_{m+1}}\right)-\frac{3}{4}\right]\right. \\ &\quad \left.+\sum_{i=1}^{m}\left(\rho_i^4\ln\left(\frac{r_{i+1}}{r_i}\right)+\left(\rho_i^2-\rho_{i-1}^2\right)r_i^2\right)\right] \end{aligned} \tag{5}$$

where r_{m+1} is an arbitrary value, introduced to obtain a more compact notation of p_{tf}. An expression for $\rho_i(r_1, r_2,\ldots,r_m)$ will be derived in subsection 2.1.5.

2.1.2. Contact resistance loss at the fingers.

The total current produced in segment i is

$$I_i = \frac{\pi}{2n}J_{\mathrm{mp}}\left(\rho_i^2-\rho_{i-1}^2\right) \tag{6}$$

and the contact resistance for this segment is

$$R_{\mathrm{cf},i} = \frac{n\rho_{\mathrm{c}}}{\pi W_{\mathrm{f}}r_i} \tag{7}$$

where ρ_{c} is the specific contact resistance between the grid metal and the top layer of the cell, and W_{f} is the finger width. The power loss due to contact resistance for this segment is given by

$$P_{\mathrm{cf},i} = I_i^2R_{\mathrm{cf},i} = \frac{\pi J_{\mathrm{mp}}^2\rho_c}{4nW_{\mathrm{f}}}\frac{\left(\rho_i^2-\rho_{i-1}^2\right)^2}{r_i} \tag{8}$$

The relative power loss is then given by summing the $P_{\mathrm{cf,i}}$ of all the segments and dividing it by P_{gen}, resulting in

$$\begin{aligned} p_{\mathrm{cf}} &= \frac{J_{\mathrm{mp}}\rho_c}{2V_{\mathrm{mp}}W_{\mathrm{f}}R^2}\sum_{i=1}^{m}\frac{\left(\rho_i^2-\rho_{i-1}^2\right)^2}{r_i} \\ &\equiv \lambda_{\mathrm{cf}}\sum_{i=1}^{m}\frac{\left(\rho_i^2-\rho_{i-1}^2\right)^2}{r_i} \end{aligned} \tag{9}$$

2.1.3. Metal resistance loss in the fingers.

For the infinitesimal element of length r_i dφ and width W_{f}, the resistance of the metal grid finger is given by

$$\mathrm{d}R_{\mathrm{mf}} = \rho_{\mathrm{sm}}\frac{r_i}{W_{\mathrm{f}}}\mathrm{d}\varphi \tag{10}$$

where ρ_{sm} is the sheet resistance of the grid metal. The current passing through this element is all the current generated in segment i, over the angle φ, i.e.

$$I(\varphi) = J_{\mathrm{mp}}\frac{\varphi}{2}\left(\rho_i^2-\rho_{i-1}^2\right) \tag{11}$$

The power loss due to ρ_{sm} in finger i is then calculated to be

$$P_{mf,i} = \int_0^{\frac{\pi}{n}} I^2(\varphi)\mathrm{d}R_{mf} = \frac{\pi^3 J_{mp}^2 \rho_{sm}}{12n^3 W_f}\left(\rho_i^2-\rho_{i-1}^2\right)^2 r_i^2 \quad (12)$$

The relative power loss due to the resistance in the fingers is then given by summing the $P_{mf,i}$ of all the segments and dividing it by P_{gen}, resulting in

$$p_{mf} = \frac{\pi^2 J_{mp}\rho_{sm}}{6n^2 V_{mp} W_f R^2}\sum_{i=1}^{m}\left(\rho_i^2-\rho_{i-1}^2\right)^2 r_i^2 \equiv \lambda_{mf}\sum_{i=1}^{m}\left(\rho_i^2-\rho_{i-1}^2\right)^2 r_i^2 \quad (13)$$

2.1.4. Shadowing loss due to the fingers.

The relative power loss associated with the shadowing effect is simply given by the ratio of the combined surface area of the fingers in the unit cell, and the total unit cell area, i.e.

$$p_{sf} = \frac{2W_f}{R^2}\sum_{i=1}^{m} r_i \equiv \lambda_{sf}\sum_{i=1}^{m} r_i \quad (14)$$

2.1.5. Total loss due to the fingers.

It is assumed that the optimum values for r_i and ρ_i depend much more on the losses induced by the fingers than those induced by the busbars, so they are optimised to minimise the relative power loss due to the fingers only. For a given value of m and n, each radius ρ_i will be such that the resistive losses are minimal, which means they can be found by setting

$$\frac{\partial(p_{tf}+p_{cf}+p_{mf})}{\partial\rho_i} = 0 \quad (15)$$

for $i = 1, 2, \ldots, m-1$. The only relevant solution to this is

$$\rho_i = \sqrt{a_i\rho_{i-1}^2 + b_i\rho_{i+1}^2 + c_i} \quad (16)$$

with

$$a_i \equiv \frac{\frac{\lambda_{cf}}{r_i}+\lambda_{mf} r_i}{d_i}, \quad b_i \equiv \frac{\frac{\lambda_{cf}}{r_{i+1}}+\lambda_{mf} r_{i+1}}{d_i}$$

$$c_i \equiv \lambda_{tf}\frac{r_{i+1}^2-r_i^2}{2d_i} \quad \text{and}$$

$$d_i \equiv \lambda_{tf}\ln\left(\frac{r_{i+1}}{r_i}\right) + \lambda_{cf}\left(\frac{1}{r_i}+\frac{1}{r_{i+1}}\right) + \lambda_{mf}(r_i + r_{i+1})$$

Starting with $i = 1$, gives $\rho_1(\rho_2)$, since $\rho_0 = 0$. Substituting this in Equation (16) for $i = 2$ then gives $\rho_2(\rho_3)$, after some rearranging. Repeating this process until $i = m-1$ ultimately gives $\rho_{m-1}(R)$, which can then be used to find $\rho_{m-2}(R)$. Repeating this until $i = 1$ yields the following expression for ρ_i:

$$\rho_i = \sqrt{R^2\prod_{j=i}^{m-1} B_j + C_i + \sum_{k=i+1}^{m-1}\left(C_k\prod_{j=i}^{k-1} B_j\right)} \quad (17)$$

with

$$B_j \equiv \frac{b_j}{1-a_j B_{j-1}}, \quad C_k \equiv \frac{a_k C_{k-1}+c_k}{1-a_k B_{k-1}}$$

$$\text{and} \quad B_0 \equiv C_0 \equiv 0.$$

After substituting Equation (17) for ρ_i in Equations (5,9 and 13), $p_f = p_{tf} + p_{cf} + p_{mf} + p_{sf}$ will give an expression for the total relative power loss due to the fingers, as a function of their radii. It turns out that the finger radii for which p_f is minimal cannot be obtained analytically. For this reason, the optimisation that yields the values of r_i for a given value of m was performed numerically. The optimum number of fingers and busbars, m and n, were simply found by comparing the various discrete possibilities until a minimum power loss was obtained.

2.2. Losses due to the busbars

Since the contact resistance of the busbars is approximated to be infinite, all the current enters the busbar via the grid fingers. Therefore, only the metal resistance loss and shadowing loss associated with the busbar need to be calculated.

2.2.1. Metal resistance loss in the busbars.

For the infinitesimal element of length $\mathrm{d}r_b$ and width $W_{b,i}/2$ in Figure 2, the resistance is given by

$$\mathrm{d}R_{mb} = \rho_{sm}\frac{2}{W_{b,i}}\mathrm{d}r_b \quad (18)$$

and the current passing through this element is all the current generated in the area enclosed by ρ_i, i.e.

$$I_i = \frac{\pi}{2n} J_{mp}\rho_i^2 \quad (19)$$

The relative power loss due to the resistance in the busbars can then be calculated to be

$$p_{mb} = \frac{\pi J_{mp}\rho_{sm}}{n V_{mp} R^2}\sum_{i=1}^{m}\frac{\rho_i^4(r_{i+1}-r_i)}{W_{b,i}} \equiv \lambda_{mb}\sum_{i=1}^{m}\frac{\rho_i^4(r_{i+1}-r_i)}{W_{b,i}} \quad (20)$$

where $r_{m+1} \equiv R$.

2.2.2. Shadowing loss due to the busbars.

The relative power loss due to shadowing by the busbars is given by the ratio of the combined surface area of the busbar sections in the unit cell, and the total unit cell area, i.e.

$$p_{\mathrm{sb}} = \frac{n}{\pi R^2}\sum_{i=1}^{m} W_{\mathrm{b},i}(r_{i+1}-r_i) \equiv \lambda_{\mathrm{sb}}\sum_{i=1}^{m} W_{\mathrm{b},i}(r_{i+1}-r_i) \tag{21}$$

where, again, $r_{m+1} \equiv R$.

2.2.3. Total loss due to the busbars.

The total relative power loss due to the busbars is then given by $p_{\mathrm{b}} = p_{\mathrm{mb}} + p_{\mathrm{sb}}$. As it is assumed that the optimum values for the r_i and, therefore, ρ_i depend mostly on the losses induced by the fingers, they can be taken as constants here. This means only the $W_{\mathrm{b},i}$ need to be optimised, by taking $\partial p_{\mathrm{b}}/\partial W_{\mathrm{b},i} = 0$, which yields

$$W_{\mathrm{b},i} = \sqrt{\frac{\lambda_{\mathrm{mb}}}{\lambda_{\mathrm{sb}}}}\rho_i^2 \tag{22}$$

with technological restrictions forcing a lower limit upon $W_{\mathrm{b},i}$.

2.3. Other contact grid patterns

Optimisation of the square grid has been performed according to the model described by Green [11] for fingers of uniform width, while for the inverted square grid, the model of Moore [10] for non-uniform finger spacing has been applied. For the optimisation of the radial contact grid, a modification is required to the model of Algora and Díaz [12], to allow more freedom in the number of (radial) fingers per annulus n_i and the radii of the (circular) busbars r_i. In the original approach of Algora and Díaz, all the n_i are taken to be dependent on n_m, the number of fingers in the most outer annulus, according to

$$n_i = \frac{2i-1}{2m-1}n_m \tag{23}$$

and n_m is the only number to be optimised. Similarly, only the number of busbars $m-1$ is optimised, while their radii are set according to

$$r_i = i\frac{R}{m} \tag{24}$$

In order to obtain a fair comparison with the other grid types, the pre-set relations described by Equations (23) and (24) cannot be applied, i.e. each n_i and r_i should be allowed to be optimised independently. The effects for the expressions for the various losses in the radial contact grid are given below.

2.3.1. Losses due to the fingers.

Following the approach of Algora and Díaz, one gets the following set of general equations for the relative power losses due to the fingers, for the radial contact grid:

$$p_{\mathrm{tf}} = \frac{\pi^2 J_{\mathrm{mp}}\rho_{\mathrm{st}}}{6V_{\mathrm{mp}}R^2}\sum_{i=1}^{m}\frac{r_i^4-r_{i-1}^4}{n_i^2} \tag{25}$$

$$p_{\mathrm{cf}} = \frac{\pi J_{\mathrm{mp}}\rho_c}{V_{\mathrm{mp}}W_{\mathrm{f}}R^2}\sum_{i=1}^{m}\frac{\left(r_i^2-r_{i-1}^2\right)^2}{n_i(r_i-r_{i-1})} \tag{26}$$

$$p_{\mathrm{mf}} = \frac{\pi J_{\mathrm{mp}}\rho_{\mathrm{sm}}}{5V_{\mathrm{mp}}W_{\mathrm{f}}R^2}\sum_{i=1}^{m}\frac{r_i^5-r_{i-1}^5}{n_i} \tag{27}$$

$$p_{\mathrm{sf}} = \frac{W_{\mathrm{f}}}{\pi R^2}\sum_{i=1}^{m} n_i(r_i-r_{i-1}) \tag{28}$$

Note that substituting Equations (23) and (24) into this set would result in the final expressions derived by Algora and Díaz.

2.3.2. Metal resistance loss in the busbars.

In the radial contact grid, each circular busbar has a number of fingers carrying current to (inner fingers, n_{in}) and from (outer fingers, n_{out}) it. Both the inner and outer fingers are symmetrically distributed in their respective annulus. The orientation of the sets of inner and outer fingers with respect to each other is chosen so that (at least) one inner and outer finger are aligned, because this results in a minimum resistance loss in the busbar. This is illustrated with the example of two inner fingers and three outer fingers, depicted in Figure 3. Here the two sets of fingers are misaligned by an angle φ_1, where for symmetry reasons $0 \le \varphi_1 \le \pi/6$.

In general, the total power loss due to ρ_{sm} in the busbar is

$$P'_{\mathrm{mb}} = \sum_{j=1}^{n_{\mathrm{in}}+n_{\mathrm{out}}} I_j^2 R_j = \frac{\rho_{\mathrm{sm}} r}{W_{\mathrm{b}}}\sum_{j=1}^{n_{\mathrm{in}}+n_{\mathrm{out}}} I_j^2\varphi_j \equiv c\sum_{j=1}^{n_{\mathrm{in}}+n_{\mathrm{out}}} I_j^2\varphi_j \tag{29}$$

where r and W_{b} are the radius and width of the busbar, respectively. Using Kirchoff's current law at each but one of the $N \equiv n_{\mathrm{in}} + n_{\mathrm{out}}$ junctions, a set of $N-1$ independent equations, for instance $I_{\mathrm{in},2} = I_4 - I_3$ in the example in Figure 3, can be set up. Now, the approximation that the contact

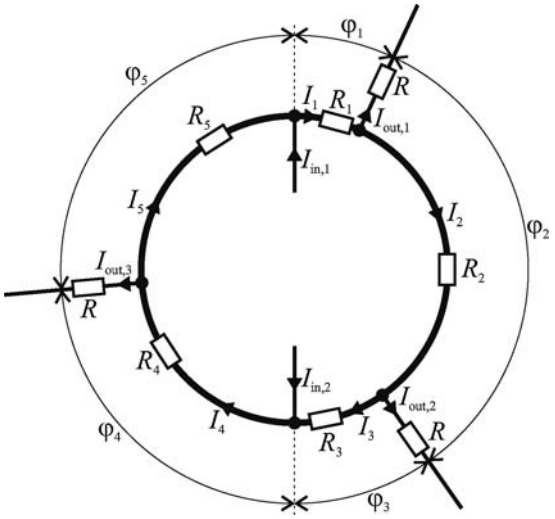

Figure 3. Schematic representation of a radial contact grid's circular busbar with two inner and three outer radial fingers. Current flows in the clockwise direction are defined as positive.

resistance of the busbar is infinite, means that

$$\sum_{j=1}^{n_{\text{in}}} I_{\text{in},j} = \sum_{j=1}^{n_{\text{out}}} I_{\text{out},j} = I \tag{30}$$

where $I = J_{\text{mp}}\pi r^2$, i.e. the total current collected in the area enclosed by the busbar. And to satisfy the requirement that each finger in a specific annulus carries the same current, as was used in the derivation of Equations (25)–(28), we get

$$I_{\text{in},j} = I/n_{\text{in}} \quad \text{and} \quad I_{\text{out},j} = I/n_{\text{out}} \tag{31}$$

(this requirement, at least for the more inner annuli, is justified by the fact that R, the resistance through the rest of the current's trajectory, will be significantly higher than any of the R_j's). Together with Equations (30) and (31), the $N-1$ independent equations can be used to express every I_j in Equation (29) in terms of I_1 and I. This gives $P'_{\text{mb}}(I_1, \varphi_1)$, which is

$$P'_{\text{mb}}(I_1, \varphi_1) = 2\pi c I_1^2 + \left(2\varphi_1 - \frac{5\pi}{3}\right) c I I_1 + \left(-\frac{2\varphi_1}{3} + \frac{43\pi}{108}\right) c I^2 \tag{32}$$

for the example in Figure 3. Since the current will distribute itself according to the path of least resistance, and thereby minimise the power loss, we know that

$$\frac{\partial P'_{\text{mb}}}{\partial I_1} = 0 \tag{33}$$

which gives $I_1(\varphi_1)$. Substituting this in Equation (32) results in $P'_{\text{mb}}(\varphi_1)$, which becomes

$$P'_{\text{mb}}(\varphi_1) = \left(-\frac{\varphi_1^2}{2\pi} + \frac{\varphi_1}{6} + \frac{11\pi}{216}\right) c I^2 \tag{34}$$

for the example in Figure 3. Setting the derivative of Equation (34) with respect to φ_1 equal to 0 turns out to yield the maximum value of φ_1 in its range (for the example in Figure 3 this is $\varphi_1 = \pi/6$), and $P'_{\text{mb}}(\varphi_1)$ is at its maximum at this value. Since there are no (local) minima, the minimum value of φ_1 in its range, i.e. $\varphi_1 = 0$, gives the minimum value for $P'_{\text{mb}}(\varphi_1) \equiv \alpha(n_{\text{in}}, n_{\text{out}}) c I^2$. This means the power loss due to metal resistance in the busbar is at a minimum if at least one inner finger is aligned with an outer finger, as claimed above. For the example in Figure 3, the resulting power loss is $P'_{\text{mb}} = \frac{11\pi}{216} c I^2$. The relative power loss in the cell due to ρ_{sm} in the busbars can be found by summing the power losses of all the busbars, and dividing it by the total power generated by the cell, i.e.

$$p_{\text{mb}} = \frac{\pi J_{\text{mp}} \rho_{\text{sm}}}{V_{\text{mp}} W_{\text{b}} R^2} \sum_{i=1}^{m-1} r_i^5 \alpha(n_i, n_{i+1}) \tag{35}$$

2.3.3. Shadowing loss of the busbars.

The relative power loss due to shadowing by the busbars is given by the ratio of the combined surface area of the busbars, and the total cell area, i.e.

$$p_{\text{sb}} = \frac{2W_{\text{b}}}{R^2} \sum_{i=1}^{m-1} r_i \tag{36}$$

3. CALCULATIONS

The numerical calculations to find the minimum relative power losses were performed for an n-on-p GaAs cell, using the parameters given in Table I. The surface area of the cell is a common size for concentrator cells, while the finger width was chosen to be a good compromise between being small, while still technologically achievable in most solar cell research labs. This finger width was also taken as the (lower limit of the) busbar widths of the radial and circular grids. The other parameters were taken from a previously reported 26.1% efficiency GaAs solar cell on substrate produced at our laboratory [13], with the sheet resistance of the grid metal based on a 5.5 μm thick silver grid, with a resistivity of $1.617\times10^{-8}\Omega$m at 25°C [14]. For concentration ratios C above 1, J_{mp} was simply multiplied by C, while the illumination was always taken to be uniform. For each condition, the optimum configuration of each type of grid pattern was determined using the Newton–Raphson method [15] and/or, for an optimisation in terms of a natural number (e.g. the number of fingers), a comparison of the various possibilities.

Table I. Values of the GaAs cell parameters used in the calculations. MPP stands for Maximum Power Point.

Parameter	Symbol	Value
Cell surface area	-	16 mm^2
Finger width	W_f	15 μm
Current density at MPP for $C=1$	J_{mp}	284 Am^{-2}
Voltage at MPP	V_{mp}	0.917 V
Sheet resistance of solar cell top layer	ρ_{st}	157 Ω/sq
Specific contact resistance between grid metal and solar cell top layer	ρ_c	3.6×10^{-10} Ωm^2
Sheet resistance of grid metal	ρ_{sm}	2.94×10^{-3} Ω/sq

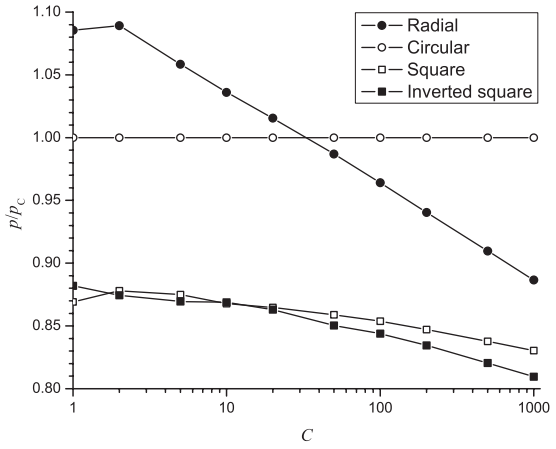

Figure 4. Normalised relative power loss of the four contact grid patterns, as a function of concentration ratio. The different types of grids were optimised for the conditions specified in Table I for each value of *C*, and the normalisation is performed w.r.t. the relative power loss of the circular grid p_c.

4. RESULTS AND DISCUSSION

Using the models described in Section 2 for the four types of contact grid patterns, their optimum configuration was determined for each concentration ratio. The resulting grid configurations for $C = 500$ are depicted in Figure 1a–d. The relative power losses of the four grid types, normalised to that of the circular contact grid, are displayed in Figure 4 as a function of *C*. As expected, the inverted square grid performs best, which was also found by Moore [10], and Algora and Díaz [12], although the difference with the square grid is minimal. The latter even surpasses the former at $C=1$ and 10, but this is due to the fact that the model used for the inverted square grid does not allow for an, in some cases more ideal, uneven number of fingers along one cell edge. For high values of *C*, and thus a high number of fingers, this effect plays a much smaller role. If one requires a round cell, the circular grid is the better choice for concentration ratios up to 30, while the radial grid performs better at higher concentration ratios.

Not imposing restrictions on the radial grid's number of fingers per annulus and on the distribution of its busbar radii (i.e. omitting Equations (23) and (24)) certainly has an effect. In the case of $C = 500$, the circular busbar radii are 37, 345 and 1053 μm and the number of radial fingers per section are 1, 9, 31 and 71. With the imposed restrictions in design as originally reported [12], this would have been 564, 1128 and 1693 μm, and 10, 30, 51 and 71, respectively, which would have resulted in a relative loss increase of 8%. So, even though the extra freedom introduced in this study makes the equations and calculations more cumbersome, it definitely pays off in this case.

Analogous to the equal distribution of busbar radii in the radial grid as applied by Algora and Díaz [12], one might also impose an equal distribution of finger radii in the circular grid. In that case, the radii would be $r_i = (2i-1/2m)R$, so that the distance from a random position on the surface to the nearest finger is never more than $R/2m$. It turns out that the radii of the circular grid optimised for $C = 500$ actually lie very close to this distribution, only the smaller radii diverge somewhat. Imposing the restriction only results in a relative loss increase of 0.4%, so for the circular grid it might be an option to impose this restriction to save calculation time in this case.

For the square grid, it is clear that allowing for non-uniform finger spacing would not improve its performance. The advantage that non-uniform finger spacing brought to the inverted square grid was negligible ($< 0.01\%$ relative for $C = 500$). This is in agreement with the results of Moore [10], and follows from the fact that the maximum deviation from the average finger spacing is less than 2.5%.

The grid patterns displayed in Figure 1 are also the optimum configurations for a GaAs cell serving as the bottom cell in a mechanical tandem subjected to an irradiance of about 1000 suns, with the top cell absorption effectively reducing the concentration ratio to 500 for the GaAs bottom cell. More generally, a comparison of the GaAs cell's different grid types in this case yields the same results as those presented in Figure 4, with *C* now corresponding to the *effective* concentration ratio experienced by the GaAs cell, and the tandem subjected to a concentration ratio of about twice this value. That is, if the GaAs bottom cell is perfectly aligned with the top cell. However, perfect alignment is not likely to be achieved in practice, so secondary shadowing effects will play a role. To determine their influence on the performance of cells with different grids, *S*, the normalised total area of two misaligned (identical) grids was calcu-

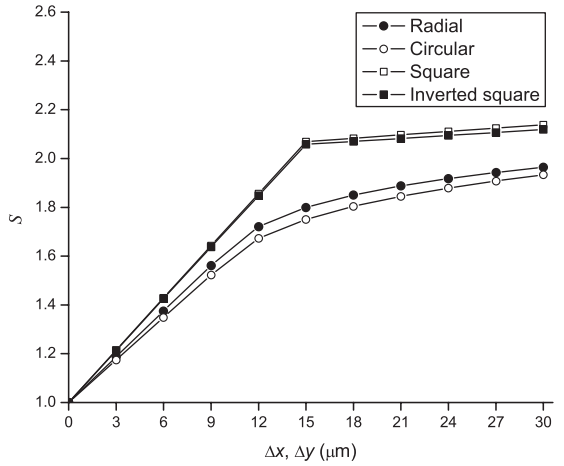

Figure 5. Normalised total contact grid area, as a function of translational misalignment, for the four grid types optimised for the conditions specified in Table I, with an effective concentration ratio of 500 for the GaAs bottom cell. The normalisation of each curve is its total grid coverage at Δx, $\Delta y = 0\,\mu$m.

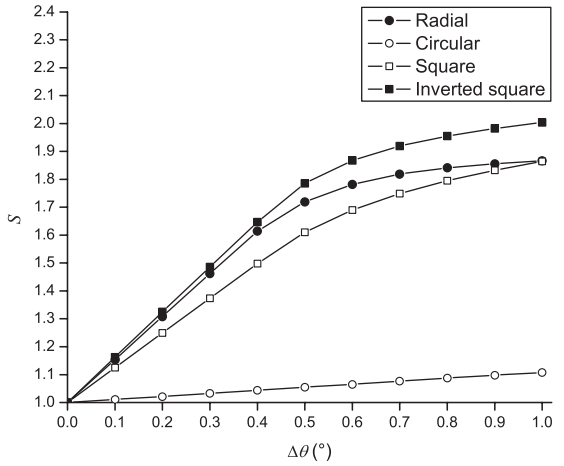

Figure 6. Normalised total contact grid area, as a function of translational misalignment, for the four grid types optimised for the conditions specified in Table I, with an effective concentration ratio of 500 for the GaAs bottom cell. The normalisation of each curve is its total grid coverage at $\Delta\theta = 0^\circ$.

lated for a series of lateral and rotational misalignments. This was done for each of the four grids optimised for the GaAs bottom cell effectively being subjected to $C = 500$, i.e. the grids displayed in Figure 1. In Figure 5, S is given for simultaneous translational misalignments in both the x and y directions, indicated by Δx and Δy, respectively, ranging from 0 to 30 μm. The sharp kinks at a displacement of 15 μm in the curves of both the square grids result from the fact that at this point, the overlap between (parallel) fingers becomes zero. The sensitivity to translational misalignment of the circular grid is comparable to that of the radial grid, and is somewhat less than those of the square grids. However, the difference is not large enough to have a significant effect on the performance ratio between the four grids, especially considering the fact that translational misalignment is not expected to exceed more than several micrometers in practise.

The difference between the four grid's values for S as a function of rotational misalignment is a lot more pronounced, as can be seen in Figure 6. Here S is given for each of the four grids, for $\Delta\theta$, the rotational misalignment around a cell's centre, ranging from 0 to 1 degrees. It is clear that the shadowing of the radial and both the square grids increases strongly with an increasing rotational misalignment and quickly approaches a doubling, while the circular grid is relatively insensitive to this effect.

Incorporating the effect of rotational misalignment into the equation for the total relative power loss (due to fingers and busbars) gives

$$p(\Delta\theta) = p_{\mathrm{tf}} + p_{\mathrm{cf}} + p_{\mathrm{mf}} + S(\Delta\theta)p_{\mathrm{sf}} + p_{\mathrm{mb}} + S(\Delta\theta)p_{\mathrm{sb}} \quad (37)$$

A plot of $p(\Delta\theta)$ for all four different grids displayed in Figure 1 is given in Figure 7. Already for $\Delta\theta \gtrsim 0.10^\circ$, the circular grid outperforms the radial grid, while the square grids are outperformed for $\Delta\theta \gtrsim 0.25^\circ$. Of course, the identical grid also has to be applied to the front and back of the top cell, influencing its performance and that of the tandem as a whole. Also note that the radial, square and inverted square grids can be optimised further by using tapered fingers, instead of fingers of uniform width. The same is true for the circular grid, but this would make it somewhat less insensitive to rotational misalignment. What should also be

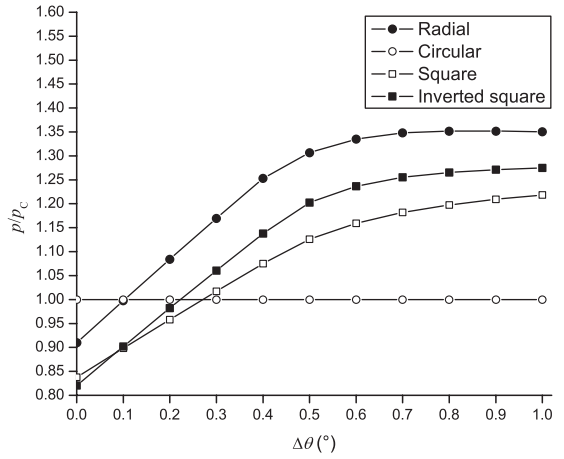

Figure 7. Normalised relative total power loss of the four contact grid patterns, as a function of rotational misalignment. The grids were optimised for the conditions specified in Table I, with an effective concentration ratio of 500 for the GaAs bottom cell. The normalisation is performed w.r.t. the circular grid.

taken into account is that the performance of the radial and circular grids (the only grids containing busbars) is somewhat conservative in comparison with the performance of the two square grids, because of the approximation that the contact resistance of the busbars is infinite. Nonetheless, the above results demonstrate that the application of a circular grid is a viable approach to minimise the losses associated with the rotational misalignment of mechanically stacked solar cells. Contemporary research in our laboratory is directed to the experimental verification of these findings.

5. CONCLUSIONS

A model was developed for a genuine circular contact grid, based on the same principles that led to previously reported models for other contact grid types. Circular grids optimised for a 16 mm^2 n-on-p GaAs cell suffer less power losses than a comparable radial grid, up to $C = 30$. At higher concentration ratios, cells with a radial grid perform better, while comparable square and inverted square grids perform better for all the considered concentration ratios, running from 1 to 1000.

In order to make a fair comparison, the models applied for the different grids were mathematically developed to a level that allowed for the same degree of freedom in design during the optimisation process. For this purpose, several pre-set conditions in the originally derived model for the radial grid were omitted and replaced by a further optimisation procedure. Without this modification, the relative power loss of the radial grid optimised for $C = 500$ would incease by 8%. For the other grids, a restriction in the degree of design freedom has much smaller effects.

For the case in which the GaAs cell serves as the bottom cell in a mechanically stacked tandem cell, the above results are valid with C corresponding to the effective concentration ratio experienced by the GaAs cell. For the four patterns optimised for the bottom GaAs cell subjected to an effective concentration ratio of 500, the effects of secondary shadowing were calculated for a range of translational and rotational misalignments. The former only showed relatively small differences between the grids, but the latter demonstrated the strength of the circular grid, since its shadowing loss hardly increases with increasing misalignment angle, while those of the other three grid types quickly approach a doubling. When these secondary shadowing effects induced by rotational misalignment are taken into account the circular grid turns out to be a viable approach to minimise the losses associated with the rotational misalignment of mechanically stacked solar cells.

ACKNOWLEDGEMENTS

This work was financially supported by the Dutch Technology Foundation (STW) under project no. 07452.

REFERENCES

1. King RR, Boca A, Hong W, Liu X-Q, Bhusari D, Larrabee D, Edmondson KM, Law DC, Fetzer CM, Mesropian S, Karam NH. Band-gap-engineered architectures for high-efficiency multijunction concentrator solar cells. *Presented at the 24th EPVSEC*, Hamburg 2009.
2. Guter W, Schöne J, Philipps SP, Steiner M, Siefer G, Wekkeli A, Welser E, Oliva E, Bett AW, Dimroth F. Current-matched triple-junction solar cell reaching 41.1% conversion efficiency under concentrated sunlight. *Applied Physics Letters* 2009; **94**: 2235041–2235043.
3. Bissels GMMW, Schermer JJ, Haverkamp EJ, Mulder P, Bauhuis GJ. Optimum bandgap calculations for a 4-terminal double tandem III–V concentrator solar cell structure. *Proceedings of 22nd EPVSEC*, Milan, 2007; 704–707.
4. Szabó N, Sağol BE, Seidel U, Schwarzburg K, Hannappel T. InGaAsP/InGaAs tandem cells for a solar cell configuration with more than three junctions. *Physica Status Solidi (RRL)* 2008; **2**: 254–256.
5. Flamand G, Zhao L, Mols Y, Van der Heide J, Poortmans J. Development of mechanically stacked multi-junction solar cells applying thin, one-side contacted III–V cells. *Proceedings of 24th EPVSEC*, Hamburg, 2009; 126–129.
6. Griggs MJ, Kayes BM, Atwater HA. P-N junction heterostructure device physics model of a four junction solar cell. *Proceedings of SPIE* 2006; **6339**: 63390D1–63390D8.
7. Van Deelen J. III–V compound solar cells: material studies and development of thin-film and tandem cells. *Ph.D. Thesis*, Radboud University Nijmegen: The Netherlands, 2008; 133–152.
8. Schermer JJ, Mulder P, Bauhuis GJ, Voncken MMAJ, Van Deelen J, Haverkamp E, Larsen PK. Epitaxial lift-Off for large area thin film III/V devices. *Physica Status Solidi(a)* 2005; **202**: 501–508.
9. Schermer JJ, Bauhuis GJ, Mulder P, Haverkamp EJ, Van Deelen J, Van Niftrik ATJ, Larsen PK. Photon confinement in high-efficiency, thin-film III–V solar cells obtained by epitaxial lift-off. *Thin Solid Films* 2006; **511**: 645–653.
10. Moore AR. An optimized grid design for a sun-concentrator solar cell. *RCA Review* 1979; **40**: 140–152.
11. Green MA. Solar Cells: Operating Principles, Technology, and System Applications. Prentice Hall: Englewood Cliffs, 1982; 153–161.
12. Algora C, Díaz V. Influence of series resistance on guidelines for manufacture of concentrator p-on-n GaAs solar

cells. *Progress in Photovoltaics: Research and Applications* 2000; **8**: 211–225.
13. Bauhuis GJ, Mulder P, Haverkamp EJ, Huijben JCCM, Schermer JJ. 26.1% thin-film GaAs solar cell using epitaxial lift-off. *Solar Energy Materials and Solar Cells* 2009; **93**: 1488–1491.
14. Lide DR (ed.). CRC Handbook of Chemistry and Physics (87th edn.). CRC Press: Boca Raton, 2006; 1239–1240.
15. Burden RL, Faires JD. Numerical Analysis (5th edn.). PWS Publishing Company: Boston, 1993; 56–69.